ACS NANO

www.acsnano.org

Two-Photon Excitation Spectroscopy of Silicon Quantum Dots and Ramifications for Bio-Imaging

Brandon J. Furey,* Benjamin J. Stacy, Tushti Shah, Rodrigo M. Barba-Barba, Ramon Carriles,* Alan Bernal, Bernardo S. Mendoza, Brian A. Korgel,* and Michael C. Downer*

Cite This: *ACS Nano* 2022, 16, 6023−6033

Read Online

ACCESS | Metrics & More | Article Recommendations | Supporting Information

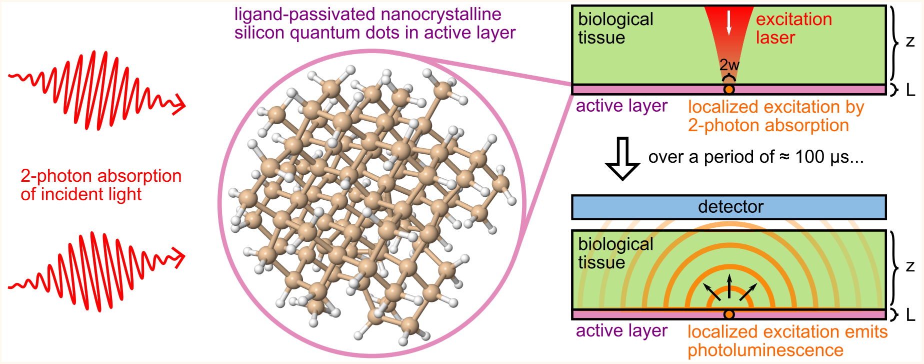

ABSTRACT: **Two-photon excitation in the near-infrared (NIR) of colloidal nanocrystalline silicon quantum dots (nc-SiQDs) with photoluminescence also in the NIR has potential opportunities in the field of deep biological imaging. Spectra of the degenerate two-photon absorption (2PA) cross section of colloidal nc-SiQDs are measured using two-photon excitation over a spectral range $1.46 < \hbar\omega < 1.91$ eV (wavelength $850 > \lambda > 650$ nm) above the two-photon band gap $E_g^{(QD)}/2$, and at a representative photon energy $\hbar\omega = 0.99$ eV ($\lambda = 1250$ nm) below this gap. Two-photon excited photoluminescence (2PE-PL) spectra of nc-SiQDs with diameters $d = 1.8 \pm 0.2$ nm and $d = 2.3 \pm 0.3$ nm, each passivated with 1-dodecene and dispersed in toluene, are calibrated in strength against 2PE-PL from a known concentration of Rhodamine B dye in methanol. The 2PA cross section is observed to be smaller for the smaller diameter nanocrystals, and the onset of 2PA is observed to be blue shifted from the two-photon indirect band gap of bulk Si, as expected for quantum confinement of excitons. The efficiencies of nc-SiQDs for bioimaging using 2PE-PL are simulated in various biological tissues and compared to efficiencies of other quantum dots and molecular fluorophores and found to be comparable or superior at greater depths.**

KEYWORDS: *two-photon absorption spectra, two-photon absorption cross section, silicon nanocrystals, quantum dots, two-photon excited photoluminescence, bioimaging*

Numerous photonic applications for nanocrystalline semiconductor quantum dots have emerged in recent years, including spin qubits in photonic networks,[1−4] quantum dot light-emitting diodes (LEDs),[5−8] in vitro and in vivo biological imaging,[9−15] and cancer therapy.[12,16,17] Some of these applications use two-photon absorption (2PA) directly to excite photoluminescence (PL), taking advantage of the availability of ultrashort, high-peak-intensity laser sources and/or high sample transparency at the excitation wavelength. In other applications, 2PA is an undesired performance inhibitor that must be understood and managed. Most prior measurements of 2PA in nanocrystalline silicon quantum dots (nc-SiQDs) have been made at a single wavelength, in ion-implanted[18] and free-standing colloidal[9,19−26] nc-SiQDs. Prior measurements of the 2PA spectrum of freestanding nc-SiQDs do not characterize the sample sufficiently to extract a 2PA

Received: December 22, 2021
Accepted: March 28, 2022
Published: March 31, 2022

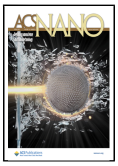

https://doi.org/10.1021/acsnano.1c11428
ACS Nano 2022, 16, 6023−6033

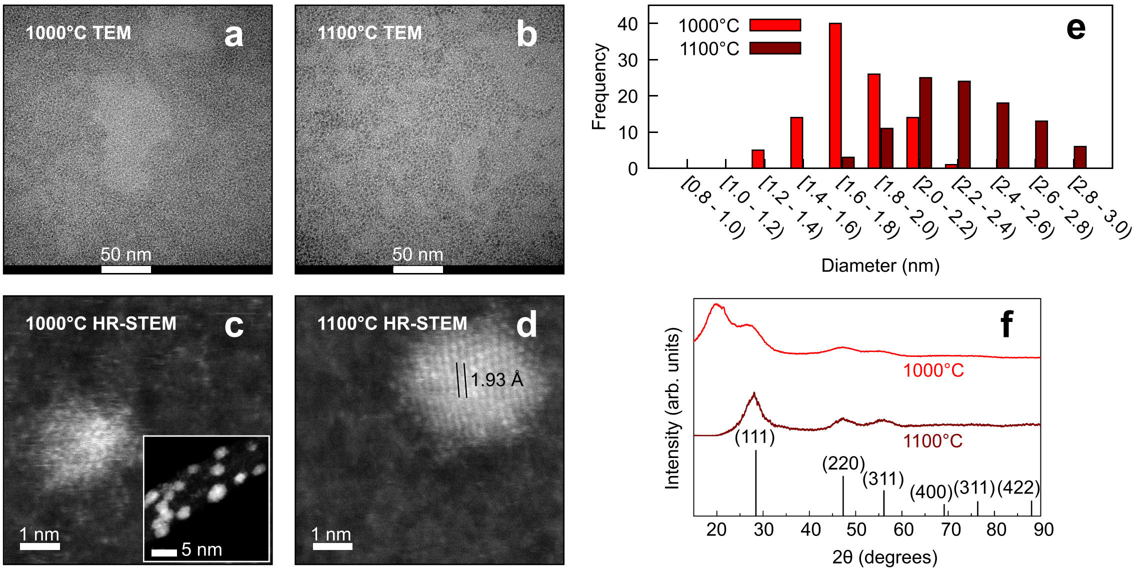

Figure 1. TEM images of nc-SiQDs annealed at 1000 °C (a) and 1100 °C (b). Aberration-corrected high-resolution dark field STEM images of a nc-SiQD annealed at 1000 °C with d = 1.8 nm (c), with inset zoomed out showing the quantum dots attached to the graphene grid, and a nc-SiQD annealed at 1100 °C with d = 3.2 nm (d). The lattice spacing of 1.93 Å is characteristic of (220) lattice spacing of Si with the (111) zone axis. Histogram of size distributions from TEM images of each nc-SiQD sample are shown in (e). XRD of nc-SiQD samples indicate crystallinity due to the presence of (111), (220), and (311) diffraction peaks in *m*3*m* crystalline Si as shown in (f).

cross section, but rather only the 2PA dispersion.[27] Here we measure two-photon excited photoluminescence (2PE-PL) spectra of free-standing colloidal nc-SiQDs[9,28,29] of diameters d = 1.8 ± 0.2 nm and d = 2.3 ± 0.3 nm over an excitation photon energy (wavelength) range $1.46 < \hbar\omega < 1.91$ eV ($650 < \lambda < 850$ nm) above the two-photon band gap $E_g^{(QD)}/2$ of the quantum dots and at a representative photon energy (wavelength) $\hbar\omega = 0.99$ eV ($\lambda = 1250$ nm) below this gap. We extract 2PA cross sections over this range from the results. Nanocrystalline SiQDs luminesce efficiently in response to excitation in this range, a feature that bioimaging applications such as two-photon excitation microscopy exploit.[9−12,30−32] In these applications, nc-SiQDs offer nontoxicity,[33,34] aqueous solution dispersibility,[9,28,29] and size-dependent emission spectra[35,36] as advantages over photoluminescent dyes, while 2PE offers the advantage over one-photon excitation (1PE) of high tissue transparency and penetration depth at the excitation wavelength. Results presented here will aid in choosing excitation wavlength and nanocrystal size for bioimaging applications and will provide data for comparison with first-principles computations of 2PA in nc-SiQDs.

The electronic structure of nc-SiQDs consists of discrete energy levels as in molecules, rather than continuous bands as in bulk crystals.[37] The energy levels of nc-SiQDs originate primarily from quantum-confined excitons, but surface, interface, and defect states can also contribute.[38] Exciton recombination dominates red and near-infrared PL, while surface, interface, and defect states are believed to contribute to green and blue PL.[38] The latter, however, are not observed from the surface-passivated nc-SiQDs studied in this work. We will ascribe PL across the band gap of the quantum dots generically to a LUMO−HOMO transition, where LUMO (HOMO) refer to a lowest unoccupied (highest occupied) molecular orbital prior to excitation. For $d \gtrsim 2$ nm diameter, the HOMO−LUMO gap and PL quantum yield both increase with decreasing d. This tunability of the PL spectrum is attractive for many applications, although it is limited in nc-SiQDs to $\hbar\omega_{PL} < 2.1$ eV.[39]

Selection rules for excitation by one-photon absorption (1PA) and 2PA can differ. In centrosymmetric molecules, they are mutually exclusive, since 1PA electric dipole transitions are parity-forbidden while their 2PA counterparts are parity-allowed. In this case, 1PA and 2PA excite complementary states.[40] However, at room temperature the PL spectra and PL quantum yields of nc-SiQDs are nearly the same for both modes of excitation.[40] Thus, the PL state excited by 2PA is considered the same as that for 1PA at the time of emission. Therefore, monitoring the spectrally integrated 2PE-PL spectra as a function of incident light intensity can indirectly be used to measure the 2PA cross section.[41]

RESULTS AND DISCUSSION

Characterization of 1-Dodecene-Passivated Colloidal nc-SiQDs. The nc-SiQDs studied in this work were synthesized by thermal decomposition of hydrogen silsesquioxane at annealing temperatures of 1000 and 1100 °C, which yielded nc-SiQDs with size distributions of d = 1.8 ± 0.2 nm and 2.3 ± 0.3 nm, respectively, as determined by transmission electron microscopy (TEM) [see Figure 1a,b,e]. The nc-SiQDs were passivated with 1-dodecene and dispersed in toluene. Abberation-corrected high-resolution dark field scanning TEM (HR-STEM) images of nc-SiQDs annealed at 1000 and 1100 °C, including a calculation of the lattice fringe spacing, are shown in Figure 1c,d. The lattice fringe spacing was measured to be 1.93 Å, computed as the average distance over 10 atomic rows. This is characteristic of the (220) lattice spacing of Si with (111) zone axis. The accepted value for the (220) lattice spacing in Si is 1.92 Å.[42] The Si quantum dots are confirmed to be crystalline by the presence of (111), (220), and (311) diffraction peaks for each of these crystal planes in *m*3*m* crystalline Si by X-ray diffraction (XRD) [see Figure 1f]. The broad peak near 20° seen in the nc-SiQD sample annealed at 1000 °C but not in the sample annealed at 1100 °C, likely due to an artifact in the background subtraction used by the XRD instrument (see the Supporting Information, Section IV.A.2, for more details). Thermal gravimetric analysis (TGA) was performed in order to determine the relative mass of the Si core to 1-dodecene. This is necessary to relate the mass concentration of a sample to a number density such that a 2PA cross section per quantum dot can be calculated. The mass fraction vs temperature curves are shown in Supporting Information Figure 5a. The quantum yields (ϕ_{PL}) of the nc-SiQDs were determined by comparing the integrated 1PE-PL emission spectra to that of a known reference standard, RhB in anhydrous ethanol. The ratio of the gradient of the trendline of luminescence intensity vs absorbance of nc-SiQDs to that of RhB is proportional to the quantum yield. The calculated quantum yields for the nc-SiQDs in this study are $\phi_{\mathrm{PL}} = 0.064$ for $d = 1.8 \pm 0.2$ nm and $\phi_{\mathrm{PL}} = 0.060$ for $d = 2.3 \pm 0.3$ nm. The molar absorptivities of the nc-SiQD samples were calculated and are shown in Supporting Information Figure 5e and the molar absorptivity of RhB from Du et al.[43] is shown in Supporting Information Figure 5f.

2PE-PL Measurements. We obtained two-photon excited PL spectra using laser pulses from an optical parametric amplifier (OPA). The output power of the OPA is sufficient to observe 2PE-PL except in the range $0.99 < \hbar\omega < 1.46$ eV, where operation switches from second-order frequency mixing of the signal to second harmonic generation (SHG) from the idler. The PL spectra of the samples were recorded as a function of incident pulse energy. An example of 2PE-PL spectra for the nc-SiQD samples and RhB dye excited at $\hbar\omega = 1.55$ eV is shown in Figure 2. The 2PE-PL spectral shape did not differ from that for 1PE-PL (see the Supporting Information, Section V). The observed spectra $S_{\mathrm{tot}}(E) = S_{\mathrm{L}}(E) + S_{\mathrm{PL}}(E)$ include scattered laser light in addition to the PL emitted from the sample, and since the laser line shape sometimes overlaps with the PL spectra, this has to be removed. The PL spectra $S_{\mathrm{PL}}(E)$ is proportional to the PL photon number within a photon energy bin of width dE centered at E. It can be empirically modeled as a sum of two Gaussian peaks and the laser line shape $S_{\mathrm{L}}(E)$ is modeled as a Lorentzian. The total detected spectra is then described by the sum of these spectral line shapes.

The total number of detectable emitted PL photons is given by

$$N_{\mathrm{PL}} = \int_{E_-}^{E_+} S_{\mathrm{PL}}(E)\,\mathrm{d}E \tag{1}$$

where $E_- = 1.24$ eV and $E_+ = 6.20$ eV are the detector limits for the spectrometer. The line shape fitting parameters for the samples studied in this work are tabulated in the Supporting Information, Section VI.B.

The number N_{PL} of detected PL photons from a single excitation pulse is directly related to the excited state population N_{e} after the pulse has propagated through the sample, $N_{\mathrm{PL}} = f_{\mathrm{det}}\phi_{\mathrm{PL}}N_{\mathrm{e}}$, where f_{det} characterizes the collection efficiency of the detector and ϕ_{PL} is the PL quantum yield. The excited state population is driven by 2PA for which the attenuation of the incident beam with propagation distance z is quadratic in its incident intensity $I(z, r, t)$,

$$\frac{\mathrm{d}I(z, r, t)}{\mathrm{d}z} = -\beta[I(z, r, t)]^2, \tag{2}$$

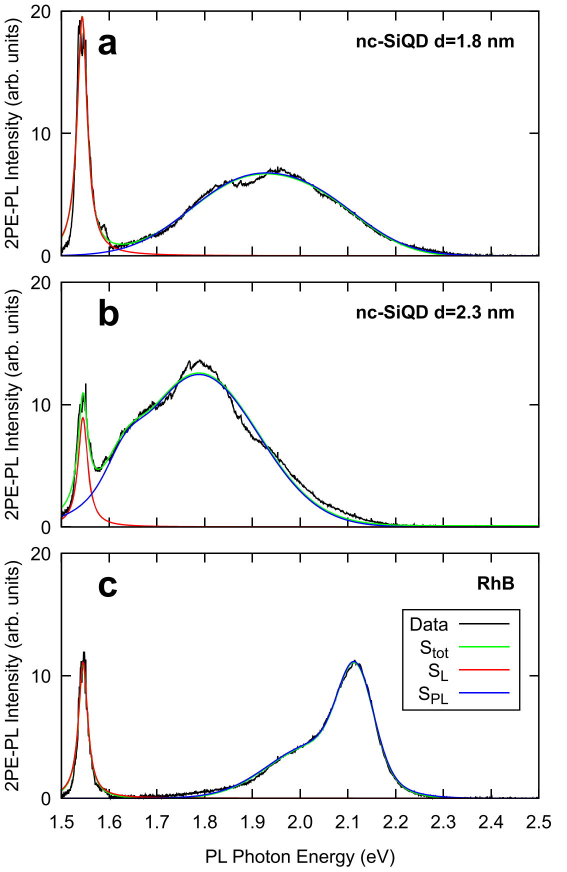

Figure 2. 2PE-PL spectra observed at excitation $\hbar\omega = 1.55$ eV (black) with total fit (green) accounting for the laser line shape (red) and 2PE-PL spectra (blue): (a) nc-SiQD sample $d = 1.8 \pm 0.2$ nm with incident pulse energy $\varepsilon_{\mathrm{P}} = 3.735 \pm 0.008$ μJ; (b) nc-SiQD sample $d = 2.3 \pm 0.3$ nm with $\varepsilon_{\mathrm{P}} = 3.804 \pm 0.008$ μJ; (c) RhB dye with $\varepsilon_{\mathrm{P}} = 3.712 \pm 0.008$ μJ. The small shoulders observed in (a) and (b) are an artifact of the spectrometer due to modulations caused by an etalon (refer to the Supporting Information, Section V and Section VI.A).

where $\beta = \sigma n_{\mathrm{g}}$ is the 2PA coefficient, σ is the 2PA cross section, and n_{g} is the ground state population density. Here we neglect free-carrier and linear absorption. ϕ_{PL} for the samples can be assumed to be the same as measured using one-photon excitation since the PL emission spectra of the two excitation channels do not appreciably differ.[40,41] The value of f_{det} can then be determined from fitting the intensity dependence of the PL from a reference standard for which ϕ_{PL}, σ, and n_0 are known. Thus, σ for the samples can be determined relative to the reference standard.

We can model the excitation of nc-SiQDs by 2PA as an effective two-level molecular system as long as the populations of higher energy excited states rapidly transition to the LUMO. The time rates-of-change of the excited (n_{e}) and ground state population densities are described by

$$\frac{\mathrm{d}n_{\mathrm{e}}(z, r, t)}{\mathrm{d}t} = \frac{\beta[I(z, r, t)]^2}{2\hbar\omega} - \Gamma n_{\mathrm{e}}(z, r, t) \tag{3}$$

$$\frac{\mathrm{d}n_{\mathrm{g}}(z, r, t)}{\mathrm{d}t} = -\frac{\mathrm{d}n_{\mathrm{e}}(z, r, t)}{\mathrm{d}t} \tag{4}$$

where $\hbar\omega$ is the photon energy of the excitation pulse and Γ is the recombination rate. The initial conditions are $n_{\mathrm{e}}(z, r, -\infty)$

$= 0$ and $n_g(z, r, -\infty) = n_0$, where n_0 is the nc-SiQD number density and $t = 0$ corresponds to the arrival of the driving pulse peak. The recombination times of the samples in this work are on the order of ns to μs, which is much longer than the time scale of a laser pulse of $\tau_g \sim 100$ fs but much shorter than the laser repetition period of $1/f_{\text{rep}} = 1$ ms, i.e., $f_{\text{rep}} \ll \Gamma \ll 1/\tau_g$. Thus, recombination can be neglected on the time scale of a pulse and the sample can be considered to be fully relaxed before the arrival of a subsequent pulse.

We assume a Gaussian spatiotemporal laser pulse profile with peak on-axis intensity I_0 and a sample thickness shorter than the Rayleigh range. The solution to eq 3 for this intensity profile, neglecting depletion of the ground state and pump beam, can then be integrated over volume to find the excited state population. This can then be related to the number of detected PL photons, which are emitted as excitons radiatively recombine across the HOMO−LUMO gap. This "lowest order" solution is quadratic with incident intensity.

We can calculate figures of merit for the validity of this model by estimating the fraction of absorbed photons on the beam axis $\Delta_{\text{ph}} \approx \sigma n_0 z I_0/\sqrt{2}$ and the fraction of excited molecules on the beam axis $\Delta_m \approx \sqrt{\pi}\sigma I_0{}^2\tau_g/(4\hbar\omega)$,[41] where w is the beam radius and $\tau_g = \tau_{\text{FWHM}}/\sqrt{2\ln 2}$ is the Gaussian pulse duration parameter expressed in terms of the FWHM pulse duration. In this work, we find that $\Delta_m < 3\%$ always, and thus neglecting depletion of the ground state is a valid assumption. However, $\Delta_{\text{ph}} < 3\%$ sometimes, but not always. In cases where pump depletion is significant, we can expand the solution about $\beta z I_0 \approx 0$ to higher orders giving

$$N_{\text{PL}} = -\frac{\pi^{3/2} f_{\text{det}}\phi_{\text{PL}} w^2 \tau_g I_0}{2^{5/2}\hbar\omega} \lim_{N\to\infty} \sum_{j=1}^{N} \frac{(-\sigma n_0 z I_0)^j}{(j+1)^{3/2}} \tag{5}$$

where the higher order terms account for pump depletion. The data are fit to eq 5 with $N = 1$ and again with $N = 2$, and if the variation in the fit parameter σ between each fit is below a threshold of 1%, then the result for the $N = 1$ case is reported; if the variation is larger, then the fit is repeated, comparing successively higher order terms until the fit parameter converges. An example of this analysis is shown in Figure 3 at $\hbar\omega = 1.55$ eV. The fit parameters are tabulated in the Supporting Information, Section VI.D.

2PA Cross Section Spectra. The values of the 2PA cross sections σ of the nc-SiQD samples relative to the RhB reference standard were measured over the range $0.99 < \hbar\omega < 1.91$ eV. The resulting spectra, based on RhB 2PA cross sections from Makarov et al.,[44] are shown in Figure 4b. The values and their standard errors are tabulated in the Supporting Information, Section VI.D. The error bars are propagated from the statistical uncertainties in the fit parameters, the reported uncertainties in the 2PA cross section of the reference RhB,[44] and the statistical uncertainties in the measured number densities (refer to the Supporting Information, Section VI.C). The 2PA cross section of nc-SiQDs increases by almost a factor of 1000 between 0.99 and 1.46 eV and continues to monotonically increase by about a factor of 10 between 1.5 and 1.9 eV. The 1PA molar absorptivity $\varepsilon(\hbar\omega)$ spectra are shown in Figure 4a for comparison of the dispersion to the 2PA spectra. The absorption in both channels increases monotonically with excitation photon energy but differs in quantitative details.

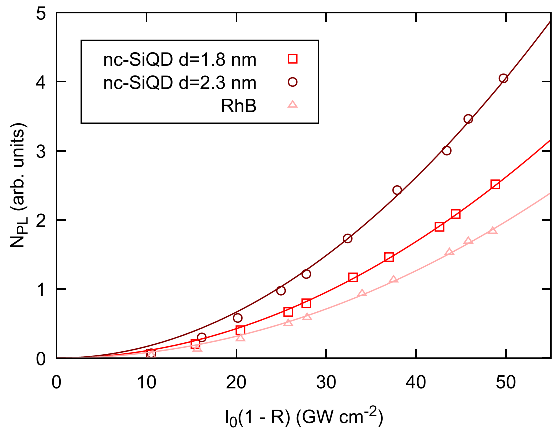

Figure 3. N_{PL} vs $I_0(1 - R)$ at $\hbar\omega = 1.55$ eV for nc-SiQD sample $d = 1.8$ nm (red squares), nc-SiQD sample $d = 2.3$ nm (dark red circles), and reference standard RhB (light red triangles) and corresponding fits to eq 5 with $N = 2$ (red curve), $N = 2$ (dark red curve), and $N = 1$ (light red curve).

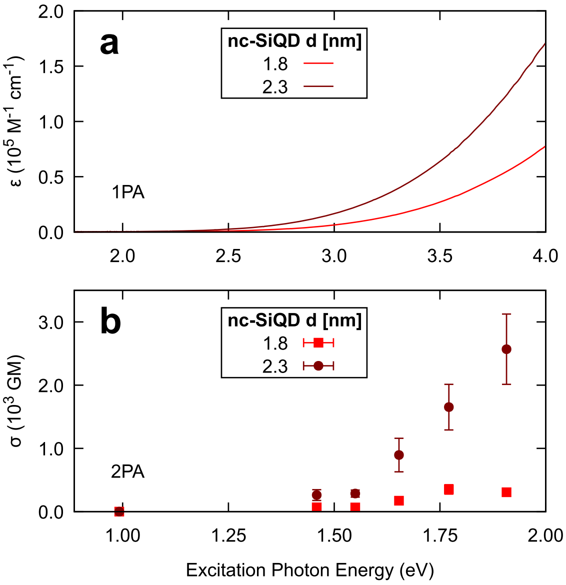

Figure 4. (a) 1PA molar absorptivity $\varepsilon(\hbar\omega)$ spectra of nc-SiQDs shown with red and dark red curves. (b) 2PA cross section $\sigma(\hbar\omega)$ spectra in units of 10^3 GM (1 Göppert−Mayer $= 10^{-50}$ cm^4 s photon^{-1}) of nc-SiQDs (red and dark red points), measured relative to RhB and then converted to absolute values using RhB cross sections from Makarov et al.[44]

The 2PA cross section can be related to an effective 2PA coefficient $\beta = \sigma n_0$ for a material with volume fraction $V_{\text{frac}} = n_0 V_{\text{QD}} = 1$, where n_0 is the quantum dot number density and $V_{\text{QD}} = (\pi/6)d^3$ is the volume of the core of a quantum dot of diameter d. This can then be used to compare how the 2PA spectra of nc-SiQDs compare to bulk Si spectra (refer to Figure 5). Bulk Si has a two-photon indirect band gap of $E_g/2 = 0.56$ eV and two-photon direct band gap of $E_0'/2 = 1.75$ eV. The 2PA cross section of nc-SiQDs increases by a factor of ≈10 between 1.5 and 1.9 eV, before the two-photon direct band gap of bulk Si. The large increase in 2PA cross section of the nc-SiQDs between 0.99 and 1.46 eV is consistent with a blue shifting in the onset of absorption with decreasing nanocrystal size, which in the limit of bulk Si occurs at the two-photon indirect band gap. The HOMO−LUMO gap has been

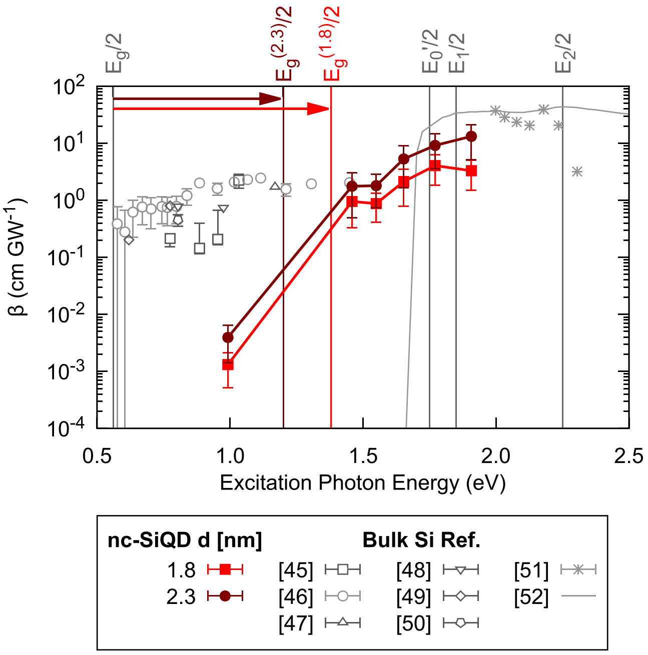

Figure 5. Degenerate 2PA coefficient $\beta(\hbar\omega)$ spectra in units of cm GW^{-1} for nc-SiQDs with volume fraction $V_{\text{frac}} = 1$ (red and dark red solid points). Dashed red and dark red lines are guides to the eye. Experimental results for bulk Si in the literature are shown with gray open symbols.[45−51] When error bars are smaller than the size of the symbol, they are omitted. Transitions in bulk Si between $E_g/2 < \hbar\omega < E_0'/2$ are indirect. The blue shifts of the 2PA band edges of the nc-SiQD samples from that of bulk Si are indicated with horizontal arrows between $E_g/2$ for bulk Si and the empirically derived HOMO−LUMO gaps for nc-SiQDs ($E_g^{(1.8,2.3)}$). Ab initio calculations for bulk Si in the literature for direct transitions above E_0' are also shown (gray curve)[52] along with the $E_1/2$ and $E_2/2$ critical points.

empirically observed to follow the trend $E_g \approx E_g^{\text{bulk}} + 2.96/d$, for E_g in eV and d in nm, where $E_g^{\text{bulk}} = 1.12$ eV is the indirect band gap of bulk Si.[38] This trend holds for the onset of linear absorption in experimental measurements[28,53−56] and ab initio calculations.[38,57,58] This relation gives a rough estimation for the onset of 2PA of $E_g^{(1.8)}/2 \approx 1.38$ eV for $d = 1.8$ nm nc-SiQDs and $E_g^{(2.3)}/2 \approx 1.20$ eV for $d = 2.3$ nm nc-SiQDs. These estimates for the HOMO−LUMO gap fall within the range $0.99 < \hbar\omega < 1.46$ eV where 2PA increased by a factor of almost 1000 and thus is consistent with our results.

The magnitude of the 2PA cross section at a given excitation energy is smaller for the smaller nanocrystals in this study, i.e., $\sigma^{(1.8)}(\omega) < \sigma^{(2.3)}(\omega)$, where the superscript indicates the diameter of the nc-SiQDs in nm [see Figure 4b]. This is consistent with the trend of linear molar absorptivity dependence on nc-SiQD size[38,56] as well as previous measurements of the 2PA cross section dependence on nc-SiQD size.[9] Interestingly, the magnitude of the 2PA cross section may scale faster than the nanocrystal volume, although the error bars for the two sizes of nanocrystals do overlap. This is evident in Figure 5 as the effective 2PA coefficient $\beta^{(2.3)}(\omega) > \beta^{(1.8)}(\omega)$.

Comparing the Simulated Efficiency of 2PE-PL Biological Imaging with nc-SiQDs to Other Imaging Agents. The onset of 2PA in the near-infrared (NIR) biotransparency window, the size-tunability of the PL spectra, and the nontoxicity of nc-SiQDs make them potentially attractive for deep bioimaging applications alongside new organic dyes[59−61] and other quantum dots.[62−65] We can simulate the efficiency of nc-SiQDs in generating an observable signal with 2PE-PL in biological tissue and compare that signal to the expected signal from 2PE-PL using other quantum dots and molecular fluorophores to aid in the selection of the optimal imaging agent and excitation wavelength for a given application (see Figure 6). This simulation models a parameter $q(z)$ from which the maximum number of 2PE-PL photons that are returned to the surface of a biological tissue can be calculated from the lowest order term of eq 5 as a function of depth z of the imaging agent in the tissue. Thus, $q(z)$ is related to the brightness of the returned signal from imaging agents in a given biological tissue as a function of depth. Comparing the values of $q(z)$ from one agent to another makes the assumption that the excitation wavelength is chosen to maximize the returned signal and that all other parameters, such as $f_{\text{det}}(E_0)$, n_0, L, I_0, etc., are equal. The maximum number of 2PE-PL photons which reach the surface of a biological tissue is given by

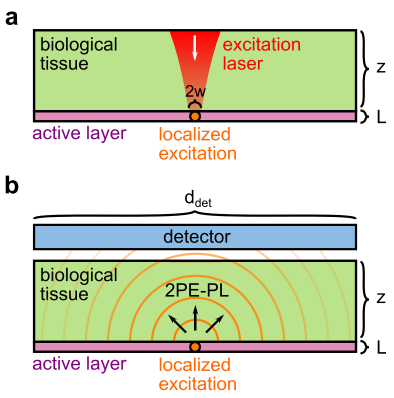

Figure 6. Model used in calculations of $q(z)$ of various imaging agents for biological imaging using 2PE-PL. An excitation laser beam transmits through the biological tissue (a) and two-photon excites a localized region near the focal volume in the active layer containing imaging agents. This localized excitation then emits isotropic 2PE-PL (b), which then transmits back to the surface of the biological tissue to be collected by a detector.

$$\max_{E_{\text{excite}}} N_{\text{PL}}^{(\text{surface})}(z) = \frac{\pi}{16} f_{\text{det}}(E_0) n_0 L w^2 \tau_g I_0^2 q(z) \tag{6}$$

Here, E_{excite} is the excitation photon energy, $f_{\text{det}}(E_0) = \phi_{\text{det}}(E_0)\Omega_{\text{det}}/(2\pi)$, $\phi_{\text{det}}(E_0)$ is the detector quantum efficiency, Ω_{det} is the detector collection solid angle, and L is the thickness of the active layer where imaging agents are present. This model assumes that PL emission radiates from a point source at the focal volume and that $d_{\text{det}} \gg z \gg w, L$, where d_{det} is the detector diameter. The detector quantum efficiency is assumed not to vary rapidly over the PL spectra, and we model the PL spectral irradiance as Gaussian peaks with a center position at E_0 and peak full width at half-maximum (fwhm) ΔE_0.

We can express the parameter $q(z)$ in units of J^{-2} cm^4 s as

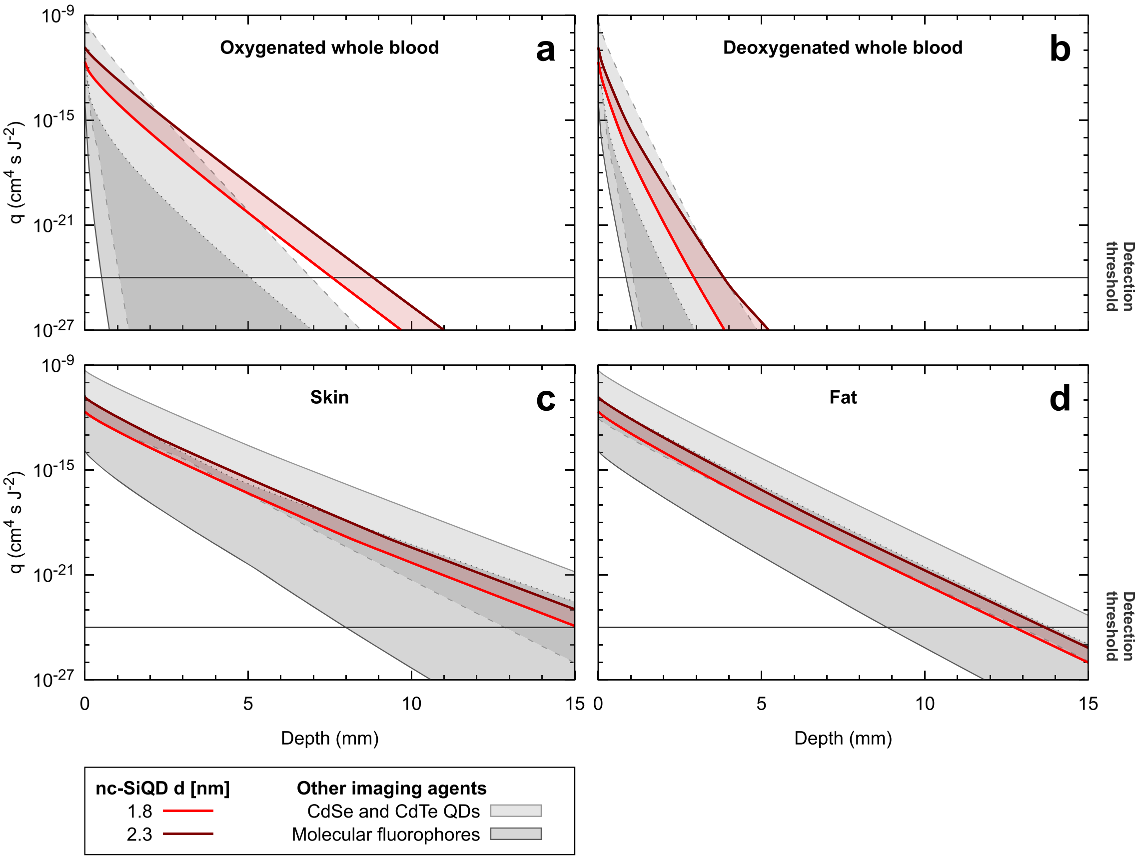

Figure 7. Simulated $q(z)$ excited by 2PA at optimal excitation wavelength for various imaging agents, including the samples measured in this work, as a function of depth z into biological tissue with associated effective attenuation spectra; (a) oxygenated whole blood, (b) deoxygenated whole blood, (c) skin, and (d) fat.[66−68] The red and dark red curves correspond to nc-SiQDs (measured in this work), with the red shading between the curves to aid the eye. The light gray shaded region bounded by dashes represents the range for CdSe and CdTe quantum dots[62] and the dark gray shaded region bounded by dots represents the range for a variety of molecular fluorophores (BODIPY, Cascade Blue, Coumarin 307, DAPI, DiI, Fluorescein, Lucifer Yellow, RhB).[44,69−74] Another version of this figure can be found in Supporting Information Figure 16 with additional detail; curves for each imaging agent are identified, and the optimal excitation photon energy/wavelength is also plotted. The horizontal dashed line indicates where the returned signal is below the approximate detection threshold for typical best case scenarios (acquisition of a single photon over ≈1 s with near unitary f_{det}, f_{rep} = 1 kHz, $n_0 \approx 10^{18}$ cm^{-3}, $L \approx 1$ mm, $w \approx 100$ μm, $\tau_{\mathrm{g}} \approx 100$ fs, and $I_0 \approx 100$ GW cm^{-2}). Note that typical human skin depths are less than ≈1.5 mm; however, we plot over the same depth range as the other tissues for consistency.

$$q(z) = \max_{E_{\mathrm{excite}}} \left\{ \frac{\phi_{\mathrm{PL}}\sigma(E_{\mathrm{excite}}) \mathrm{e}^{-2\alpha_{\mathrm{bio}}(E_{\mathrm{excite}})z}}{E_{\mathrm{excite}}\Delta E_0\left[1 + \mathrm{erf}\left(\frac{E_0}{\Delta E_0}\right)\right]} \int_{E_{\mathrm{IRCO}}}^{\infty} \frac{\mathrm{e}^{-(E-E_0)^2/\Delta E_0^{\,2}}}{E} \times \left(\int_0^{\pi/2} \mathrm{e}^{-\alpha_{\mathrm{bio}}(E)z/\cos\theta} \sin\theta \, \mathrm{d}\theta \right) \mathrm{d}E \right\} \tag{7}$$

where $\alpha_{\mathrm{bio}}(E)$ is the effective linear attenuation coefficient of the biological tissue (accounting for losses due to absorption and scatter) and θ is the angle to the normal. The prefactor $\phi_{\mathrm{PL}}\sigma(E_{\mathrm{excite}})$ is the 2PE-PL efficiency at E_{excite}, $\mathrm{e}^{-2\alpha_{\mathrm{bio}}(E_{\mathrm{excite}})z}$ is the linear attenuation in the biological tissue of the square of the incident intensity, E_{excite} appears in the denominator in the conversion of σ from GM to SI units, the $\Delta E_0\left[1 + \mathrm{erf}\left(\frac{E_0}{\Delta E_0}\right)\right]$ term in the denominator is a normalization factor for the integral immediately following, and E_{IRCO} is a small but finite infrared cutoff energy. The first integral performed over dθ represents the fraction of PL at a given photon energy E that is emitted into the upper hemisphere and that transmits to the surface of the biological tissue of depth z. The next integral over dE is the fraction of emitted photons that are transmitted to the surface and accounts for the PL spectrum over which $\alpha_{\mathrm{bio}}(E)$ may vary.

The results of these simulations for the nc-SiQDs in this work, CdSe and CdTe quantum dots, and a variety of molecular fluorophores are shown in Figure 7. Details of these simulations are given in the Supporting Information, Section VII. The nc-SiQDs show comparable or superior efficiencies or, more precisely, exhibit large $q(z)$ values and the least reduction in signal with depth, $|\mathrm{d}q(z)/\mathrm{d}z|$, in oxygenated whole blood and deoxygenated whole blood compared with results for other quantum dots and molecular fluorophores simulated. Compared to the molecular fluorophores simulated, nc-SiQDs can produce a detectable signal at an approximate threshold for detection ≈2−8× deeper. Even within skin and fat, nc-SiQDs offer comparable high performance, especially for deep bioimaging. This is primarily due to two factors related to the deeper penetration depth of longer wavelength light in biological tissue; the PL emission peak of nc-SiQDs is in the NIR, and the 2PA cross section is larger in the NIR. This performance in nc-SiQDs is attained with the benefit of being biologically inert, while many of the other imaging agents compared to here are toxic. The results presented here yield potential opportunities in the field of deep bioimaging.

CONCLUSIONS

In conclusion, we characterized the 2PA cross section spectra of two different sizes of ligand-passivated and colloidally dispersed nc-SiQDs with diameters $d = 1.8 \pm 0.2$ nm and $d = 2.3 \pm 0.3$ nm using 2PE-PL as a proxy relative to the well-known reference standard of RhB over the range $0.99 < \hbar\omega < 1.91$ eV. We observed the 2PA cross section decreases with decreasing nanocrystal diameter. The HOMO−LUMO gap in the nc-SiQDs was blue shifted from the two-photon indirect band gap of bulk Si, as expected due to quantum confinement of excitons, matching the trend observed in linear absorption experiments[28,53−56] and ab initio calculations.[38,57,58] Ab initio calculations of the rotationally averaged imaginary part of the molecular third-order nonlinear optical susceptibility tensor of nc-SiQDs as a function of size could be compared to experimentally measured 2PA cross sections, and such calculations would be useful for understanding both the 2PA spectral structure and dependence on nanocrystal size. The efficiencies of nc-SiQDs for bioimaging using 2PE-PL were simulated in various biological tissues and compared to efficiencies of other quantum dots and molecular fluorophores and found to be comparable or superior at greater depths due to their NIR PL and 2PA peaks, offering a potential advancement to the field of deep bioimaging. Future experiments demonstrating a direct and systematic comparison between nc-SiQDs and other imaging agents in a realistic bioimaging situation would be useful to confirm these results.

METHODS

Sample Preparation. Hydrogen-passivated nanocrystals were synthesized by thermally decomposing hydrogen silsesquioxane, mechanically grinding the product into oxide-embedded nc-SiQDs, and then suspending the powder in an acid solution to etch away the oxide. This procedure yields hydride-terminated nc-SiQDs. Hessel et al.[56] and the Supporting Information, Sections III.A and III.B, describe the procedure in detail. The hydride-terminated nc-SiQD sample is then dispersed in 8 mL of 1-dodecene. The dispersion is heated at 190 °C for 20 h. After about 30 min of heating, the turbid brown dispersion turns to an optically clear orange dispersion, indicating passivation of the nc-SiQDs. The alkene-passivated nc-SiQDs are washed three times by precipitation with ethanol as an antisolvent (15 mL) and redispersed in 1 mL of toluene for use in experiments. Refer to the Supporting Information, Section III.C, for details of the alkene passivation procedure. The reference standard for 2PE-PL measurements in this work was RhB dye in methanol for which a fresh sample was prepared each day measurements were taken.

Sample Characterization. *Transmission Electron Microscopy.* Average nanocrystal diameters and size distributions were determined by imaging individual nanocrystals with a high-resolution TEM (JEOL Ltd. Model 2010F HR-TEM) operated at 200 kV. The particle size distributions were determined by calculating the sizes of 100 particles in each sample. See Figure 1a,b,e. Graphene-enhanced lacey carbon TEM grids were purchased from Electron Microscopy Sciences (Cat. no. GF1201). A dilute nanocrystal solution in chloroform was dropcast onto the grid and stored in a vacuum chamber overnight before imaging. Aberration-corrected scanning TEM (acSTEM) was performed using a JEOL NEOARM TEM with an 80 kV accelerating voltage and a point-to-point STEM resolution of 0.11 nm. These high-resolution acSTEM images are shown in Figure 1c,d.

X-ray Diffraction. XRD was performed on each of the nc-SiQD samples using a Rigaku R-Axis Spider diffractometer using Cu Kα radiation ($\lambda = 0.154\,18$ nm) to ascertain the crystallinity of the quantum dots. The quantum dots were deposited on a glass slide, the solvent was evaporated, and then the powder was placed on a nylon loop. Two-dimensional diffraction data were collected for 10 min while rotating the sample stage at 10°/min. 2D diffraction data were radially integrated with 2DP software and are shown in Figure 1f.

Thermal Gravimetric Analysis. TGA was performed using an automated ultramicro balance (Mettler-Toledo International, Inc. Model TGA-1) in order to determine the relative mass of the Si core to 1-dodecene. Samples were heated at a rate of 20 °C/min from 40 to 800 °C. The sample was held at 100 °C for 30 min to evaporate residual solvents and at 800 °C for 30 min to ensure all ligand had evaporated. The relative mass of the Si core to 1-dodecene in the passivated samples was determined from the remaining mass of Si and the total weight loss due to the removal of the ligands. The mass fraction vs temperature curves are shown in Supporting Information Figure 5a.

Quantum Yield Calculations. 1PE-PL, shown in Supporting Information Figure 5b, and PL excitation (PLE) spectra in the ultraviolet−visible (UV−vis) wavelength range were acquired on a fluorescence spectrophotometer (Varian, Inc. Model Cary Eclipse). UV−vis absorbance spectroscopy was performed on a UV−vis spectrophotometer (Varian, Inc. Model Cary 50 Bio UV−vis). The quantum yields (ϕ_{PL}) of the nc-SiQDs were determined by comparing the integrated 1PE-PL emission spectra to that of a known reference standard, RhB in anhydrous ethanol (with $\phi_{\mathrm{PL}} = 0.49$).[75] The quantum yield was calculated by integrating the emission spectra at five different concentrations. These are plotted against absorbance at the excitation wavelength for both the nc-SiQDs and RhB, shown in Supporting Information Figure 5c,d. The gradient of the trendline of luminescence intensity vs absorbance for both nc-SiQDs and RhB are used to compute the quantum yields of the nc-SiQDs by $\phi_{\mathrm{PL}}^{\mathrm{s}} = \phi_{\mathrm{PL}}^{\mathrm{r}}(m_{\mathrm{s}}/m_{\mathrm{r}})(n_{\mathrm{s}}/n_{\mathrm{r}})^2$, where ($\phi_{\mathrm{PL}}^{\mathrm{s}}$, $\phi_{\mathrm{PL}}^{\mathrm{r}}$) is the (sample, reference) quantum yield, (m_{s}, m_{r}) is the gradient of integrated PL vs absorbance of the (sample, reference), $n_{\mathrm{s}} = 1.496$ is the refractive index of the sample solvent (toluene), and $n_{\mathrm{r}} = 1.365$ is the refractive index of the reference solvent (ethanol).[76]

Molar Absorptivities. The molar absorptivities $\varepsilon(\omega)$ of the nc-SiQD samples were calculated by measuring the absorbances $A(\omega)$ of nc-SiQD solutions at variable concentrations and applying the Beer−Lambert Law, $A(\omega) = \varepsilon(\omega)LC$, where L is the optical path length (1 cm) and C is the nc-SiQD concentration. The molar concentrations of the nc-SiQD samples were determined by taking the average diameter as measured from TEM imagery and calculating the ligands per nanocrystal with the mass fraction measured with TGA. The molar absorptivities of the nc-SiQD samples are shown in Supporting Information Figure 5e and those of RhB from ref 43 are in Supporting Information Figure 5f. The molar absorptivities were used to determine the concentration of the samples in the 2PE-PL experiment by measuring the absorbance spectra of the samples with a spectrophotometer (PerkinElmer, Inc. Model Spectrum 400) and fitting to an empirical model for the molar absorptivity to the Beer−Lambert Law. The molar concentration C and number density n_0 of the samples are tabulated in the Supporting Information, Sections IV.B.7 and IV.B.8. Refer to the Supporting Information, Section IV.B, for additional details on these calculations.

2PE-PL Measurements. *Laser Source.* We used two-photon excited PL using laser pulses from an OPA (Light Conversion Co. Model TOPAS-C, tuning range $240 < \lambda < 2600$ nm) pumped by a 1 kHz titanium-doped sapphire regenerative amplifier (Coherent, Inc. Model Libra HE USP). Excitation pulses passed through spectral, spatial, and polarization filters tailored for each excitation wavelength to ensure well-defined pulse spectra, Gaussian transverse beam profiles, and linear polarization throughout the tuning range.

Spatiotemporal Profile Characterization. The pulse duration was measured by performing a SHG two-beam second-order autocorrelation using a barium borate crystal placed in the sample position.[45] The average power was measured with a Si photodiode (PD) head

(Coherent Model FieldMate, 650−1100 nm) or a thermal head (Coherent Model FieldMate, 1200−2000 nm) and used to calibrate the reference photodiode detector. The beam radius at the sample position was measured using an automated knife-edge technique. See the Supporting Information, Section II, for details on characterization of the pulse duration and characterization of the beam radius.

Experimental Setup. A continuously variable neutral density (ND) filter wheel controls the incident intensity. A beam splitter reflects 4% to a reference photodiode detector (Thorlabs, Inc. Model DET100A for 325−1100 nm, Thorlabs PDA30G for 1200−1400 nm) to monitor the incident laser power. The output of the photodiode detector was integrated and held for each pulse until the next trigger by a gated integrator (Stanford Research Systems Co. Model SR250).[45] A plano-convex lens (with focal length f = 500 mm) focuses the transmitted beam into the sample, which is contained in a 1 mm path length optical glass cuvette (Hellma GmbH & Co. KG Model Z802689). A collection lens and fiber coupler injects a portion of the emitted PL into a 0.22 NA, $250 < \lambda < 1200$ nm, $d = 200$ μm core, double clad, multimode optical fiber patch cable (Thorlabs Model FG200UCC). The spectra is then analyzed using a compact CCD spectrometer (Thorlabs Model CCS200) and recorded by computer. See the Supporting Information, Section I, for further details on the experimental setup.

Samples. The samples were placed in a cuvette holder and the PL spectra recorded as a function of incident pulse energy. Care was taken to ensure that the incident intensity was kept below the threshold for bubble formation in the colloidal sample, as bubbles of vaporized solvent significantly increased scattered light.

Simulations of Efficiency of 2PE-PL Bio-Imaging. The efficiency of a detectable signal from 2PE-PL in biological imaging applications is simulated using eq 7, where the optimal excitation photon energy/wavelength is chosen to maximize eq 6. A detailed version of Figure 7 can be found in Supporting Information Figure 16 with curves for each imaging agent identified and the optimal excitation photon energy/wavelength also plotted. Effective attenuation coefficients for biological tissues were obtained from Smith et al.,[66] Friebel et al.,[67] and Bashkatov et al.[68] In this simulation, we model the PL spectrum of the samples as a Gaussian peak with a center position at E_0 and peak fwhm ΔE_0, unique to each sample. The simulated samples include nc-SiQDs from this work, CdSe and CdTe quantum dots from Pu et al.,[62] and various molecular fluorophores in the literature: RhB 2PA spectrum and ϕ_{PL} from Makarov et al.[44] and PL spectrum from this work; BODIPY, Cascade Blue, Coumarin 307, DAPI, DiI, Fluorescein, and Lucifer Yellow 2PA spectra and ϕ_{PL} from Xu et al.[69] and corresponding PL spectra for Cascade Blue, DAPI, and Fluorescein from Shapiro;[70] PL spectrum for BODIPY from Schmitt et al.;[71] PL spectrum for Coumarin 307 from Mannekutla et al.;[72] PL spectrum for DiI from *The Molecular Probes Handbook*;[73] and the PL spectrum for Lucifer Yellow from omlc.[74] These data are also compiled in the Supporting Information, Section VII.

ASSOCIATED CONTENT

Supporting Information

The Supporting Information is available free of charge at https://pubs.acs.org/doi/10.1021/acsnano.1c11428.

> 2PE-PL experimental setup diagram; spatiotemporal profile characterization, knife-edge transect to characterize transverse beam profile, table of beam radii, noncollinear two-beam SHG second-order autocorrelation; details of sample preparation and characterization, model of nc-SiQD, absorbance spectra, table of molecular weight calculations, molar absorptivity spectra, and table of fit parameters; comparison of PL spectra by excitation channel; data archive, tables of empirical 2PE-PL spectra, 2PA cross sections, 2PA figures of merit, and N_{PL} vs $I_0(1 - R)$ graphs; details of the simulations of efficiency of 2PE-PL bioimaging, graphs of simulated $q(z)$ excited by 2PA and optimal excitation photon energy/wavelength and tables of spectral data; and the relationship of 2PA cross section to the isotropic molecular third-order nonlinear optical susceptibility tensor (PDF)

AUTHOR INFORMATION

Corresponding Authors

Brandon J. Furey − *Department of Physics, University of Texas at Austin, Austin, Texas 78712, United States;* Present Address: Institut für Experimentalphysik, Universität Innsbruck, Technikerstraße 25/4, Innsbruck, Austria A-6020; orcid.org/0000-0001-7535-1874; Email: furey@utexas.edu

Ramon Carriles − *Centro de Investigaciones en Óptica, A.C., León, Gto. 37150, México;* orcid.org/0000-0001-8347-8111; Email: ramon@cio.mx

Brian A. Korgel − *McKetta Department of Chemical Engineering, University of Texas at Austin, Austin, Texas 78712, United States; Texas Materials Institute, University of Texas at Austin, Austin, Texas 78712, United States;* orcid.org/0000-0001-6242-7526; Email: korgel@che.utexas.edu

Michael C. Downer − *Department of Physics, University of Texas at Austin, Austin, Texas 78712, United States;* orcid.org/0000-0003-1478-4582; Email: downer@physics.utexas.edu

Authors

Benjamin J. Stacy − *McKetta Department of Chemical Engineering, University of Texas at Austin, Austin, Texas 78712, United States; Texas Materials Institute, University of Texas at Austin, Austin, Texas 78712, United States;* orcid.org/0000-0002-7434-7205

Tushti Shah − *McKetta Department of Chemical Engineering, University of Texas at Austin, Austin, Texas 78712, United States;* orcid.org/0000-0002-7334-1979

Rodrigo M. Barba-Barba − *Centro de Investigaciones en Óptica, A.C., León, Gto. 37150, México;* orcid.org/0000-0003-1705-2686

Alan Bernal − *Centro de Investigaciones en Óptica, A.C., León, Gto. 37150, México;* orcid.org/0000-0002-6945-8429

Bernardo S. Mendoza − *Centro de Investigaciones en Óptica, A.C., León, Gto. 37150, México;* orcid.org/0000-0002-8546-0262

Complete contact information is available at: https://pubs.acs.org/10.1021/acsnano.1c11428

Notes

The authors declare no competing financial interest.

An open-access preprint of this manuscript is available: B. J. Furey, B. Stacy, T. Shah, R. M. Barba-Barba, R. Carriles, A. Bernal, B. S. Mendoza, B. A. Korgel, and M. C. Downer. Two-Photon Excitation Spectroscopy of Silicon Quantum Dots and Ramifications for Bio-Imaging. 2021, arXiv:2112.12241. https://arxiv.org/abs/2112.12241 (accessed December 22, 2021).

ACKNOWLEDGMENTS

This research was funded by Robert A. Welch Foundation Grants F-1038 and F-1464 and partially supported by the National Science Foundation through the Center for Dynamics and Control of Materials; an NSF MRSEC under Cooperative Agreement No. DMR-1720595. B. S. Mendoza acknowledges support from Consejo Nacional de Ciencia y Tecnología, México (Grant No. A1-S-9410). The majority of the experimental work was performed at the Laboratorio de Óptica Ultrarrápida at Centro de Investigaciones en Óptica, A.C. in León, México. The authors thank E. Noé-Arias (Centro de Investigaciones en Óptica) for data acquisition program development, M. Olmos-López (Centro de Investigaciones en Óptica) for access to spectrophotometer, and J. Clifford (University of Texas at Austin) and the Centro de Investigaciones en Óptica Machine Shop for machining assistance and part fabrication.

REFERENCES

(1) Kim, D.; Carter, S.; Greilich, A.; Bracker, A.; Gammon, D. Ultrafast Optical Control of Entanglement Between Two Quantum-Dot Spins. *Nat. Phys.* **2011**, *7*, 223−229.

(2) Press, D.; Greve, K.; McMahon, P.; Ladd, T.; Friess, B.; Schneider, C.; Kamp, M.; Höfling, S.; Forchel, A.; Yamamoto, Y. Ultrafast Optical Spin Echo In a Single Quantum Dot. *Nat. Photonics* **2010**, *4*, 367−370.

(3) Yamamoto, Y.; Ladd, T.; Press, D.; Clark, S.; Sanaka, K.; Santori, C.; Fattal, D.; Fu, K.; Höfling, S.; Reitzenstein, S.; et al. Optically Controlled Semiconductor Spin Qubits for Quantum Information Processing. *Phys. Scr.* **2009**, *T137*, 014010.

(4) Greve, K.; Yu, L.; McMahon, P.; Pelc, J.; Natarajan, C.; Kim, N.; Abe, E.; Maier, S.; Schneider, C.; Kamp, M.; et al. Quantum-Dot Spin-Photon Entanglement *via* Frequency Downconversion to Telecom Wavelength. *Nature* **2012**, *491*, 421−425.

(5) Choi, M.; Yang, J.; Hyeon, T.; Kim, D. Flexible Quantum Dot Light-Emitting Diodes for Next-Generation Displays. *npj Flex. Electron.* **2018**, *2*, 10.

(6) Yang, J.; Choi, M.; Kim, D.; Hyeon, T. Designed Assembly and Integration of Colloidal Nanocrystals for Device Applications. *Adv. Mater.* **2016**, *28*, 1176−1207.

(7) Dai, X.; Deng, Y.; Peng, X.; Jin, Y. Quantum-Dot Light-Emitting Diodes for Large-Area Displays: Towards the Dawn of Commercialization. *Adv. Mater.* **2017**, *29*, 1607022.

(8) Pimputkar, S.; Speck, J.; Denbaars, S.; Nakamura, S. Prospects for LED Lighting. *Nat. Photonics* **2009**, *3*, 180−182.

(9) Furey, B.; Silbaugh, D.; Yu, Y.; Guillaussier, A.; Estrada, A.; Stevens, C.; Maynard, J.; Korgel, B.; Downer, M. Measurement of Two-Photon Absorption of Silicon Nanocrystals in Colloidal Suspension for Bio-Imaging Applications. *Phys. Status Solidi B* **2018**, *255*, 1700501−1700507.

(10) Kim, D.; Kang, J.; Wang, T.; Ryu, H.; Zuidema, J.; Joo, J.; Kim, M.; Huh, Y.; Jung, J.; Ahn, K.; et al. Two-Photon *In Vivo* Imaging with Porous Silicon Nanoparticles. *Adv. Mater.* **2017**, *29*, 1703309.

(11) Chandra, S.; Ghosh, B.; Beaune, G.; Nagarajan, U.; Yasui, T.; Nakamura, J.; Tsuruoka, T.; Baba, Y.; Shirahata, N.; Winnik, F. Functional Double-Shelled Silicon Nanocrystals for Two-Photon Fluorescence Cell Imaging: Spectral Evolution and Tuning. *Nanoscale* **2016**, *8*, 9009−9019.

(12) Kharin, A.; Lysenko, V.; Rogov, A.; Ryabchikov, Y.; Geloen, A.; Tishchenko, I.; Marty, O.; Sennikov, P.; Kornev, R.; Zavestovskaya, I.; et al. Bi-Modal Nonlinear Optical Contrast from Si Nanoparticles for Cancer Theranostics. *Adv. Opt. Mater.* **2019**, *7*, 1801728−1801736.

(13) Sakiyama, M.; Sugimoto, H.; Fujii, M. Long-Lived Luminescence of Colloidal Silicon Quantum Dots for Time-Gated Fluorescence Imaging in the Second Near Infrared Window in Biological Tissue. *Nanoscale* **2018**, *10*, 13902−13907.

(14) McVey, B.; Tilley, R. Solution Synthesis, Optical Properties, and Bioimaging Applications of Silicon Nanocrystals. *Acc. Chem. Res.* **2014**, *47*, 3045−3051.

(15) Liang, J.; Huang, C.; Gong, X. Silicon Nanocrystals and Their Composites: Syntheses, Fluorescence Mechanisms, and Biological Applications. *ACS Sustainable Chem. Eng.* **2019**, *7*, 18213−18227.

(16) Tamarov, K.; Osminkina, L.; Zinovyev, S.; Maximova, K.; Kargina, J.; Gongalsky, M.; Ryabchikov, Y.; Al-Kattan, A.; Sviridov, P.; Sentis, M.; et al. Radio Frequency Radiation-Induced Hyperthermia Using Si Nanoparticle-Based Sensitizers for Mild Cancer Therapy. *Sci. Rep.* **2015**, *4*, 7034.

(17) Lee, C.; Kim, H.; Hong, C.; Kim, M.; Hong, S.; Lee, D.; Lee, W. Porous Silicon As an Agent for Cancer Thermotherapy Based on Near-Infrared Light Irradiation. *J. Mater. Chem.* **2008**, *18*, 4790−4795.

(18) Torres-Torres, C.; Bornacelli, J.; Rangel-Rojo, R.; García-Merino, J.; Can-Uc, B.; Tamayo-Rivera, L.; Cheang-Wong, J.; Rodríguez-Fernández, L.; Oliver, A. Photothermally Activated Two-Photon Absorption in Ion-Implanted Silicon Quantum Dots in Silica Plates. *J. Nanomater.* **2018**, *2018*, 3470167.

(19) Falconieri, M.; D'Amato, R.; Fabbri, F.; Carpanese, M.; Borsella, E. Two-Photon Excitation of Luminescence in Pyrolytic Silicon Nanocrystals. *Physica E* **2009**, *41*, 951−954.

(20) Prakash, G.; Cazzanelli, M.; Gaburro, Z.; Pavesi, L. Nonlinear Optical Properties of Silicon Nanocrystals Grown by Plasma-Enhanced Chemical Vapor Deposition. *J. Appl. Phys.* **2002**, *91*, 4607.

(21) Spano, R.; Daldosso, N.; Cazzanelli, M.; Ferraioli, L.; Tartara, L.; Yu, J.; Degiorgio, V.; Jordana, E.; Fedeli, J.; Pavesi, L. Bound Electronic and Free Carrier Nonlinearities in Silicon Nanocrystals at 1550nm. *Opt. Express* **2009**, *17*, 3941−3950.

(22) Trojánek, F.; Neudert, K.; Žídek, K.; Dohnaloá, K.; Pelant, I.; Malý, P. Femtosecond Photoluminescence Spectroscopy of Silicon Nanocrystals. *Phys. Status Solidi C* **2006**, *3*, 3873−3876.

(23) Siekierzycka, J.; Rosso-Vasic, M.; Zuilhof, H.; Brouwer, A. Photophysics of n-Butyl-Capped Silicon Nanoparticles. *J. Phys. Chem. C* **2011**, *115*, 20888−20895.

(24) Portolés, M.; Nieto, F.; Soria, D.; Amalvy, J.; Peruzzo, P.; Mártire, D.; Kotler, M.; Holub, O.; Gonzalez, M. Photophysical Properties of Blue-Emitting Silicon Nanoparticles. *J. Phys. Chem. C* **2009**, *113*, 13694−13702.

(25) Akcakir, O.; Therrien, J.; Belomoin, G.; Barry, N.; Muller, J.; Gratton, E.; Nayfeh, M. Detection of Luminescent Single Ultrasmall Silicon Nanoparticles Using Fluctuation Correlation Spectroscopy. *Appl. Phys. Lett.* **2000**, *76*, 1857−1859.

(26) Gui, R.; Jin, H.; Wang, Z.; Tan, L. Recent Advances in Optical Properties and Applications of Colloidal Quantum Dots Under Two-Photon Excitation. *Coord. Chem. Rev.* **2017**, *338*, 141−185.

(27) He, G.; Zheng, Q.; Yong, K.; Erogbogbo, F.; Swihart, M.; Prasad, P. Two- and Three-Photon Absorption and Frequency Upconverted Emission of Silicon Quantum Dots. *Nano Lett.* **2008**, *8*, 2688−2692.

(28) Hessel, C.; Rasch, M.; Hueso, J.; Goodfellow, B.; Akhavan, V.; Puvanakrishnan, P.; Tunel, J.; Korgel, B. Alkyl Passivation and Amphiphilic Polymer Coating of Silicon Nanocrystals for Diagnostic Imaging. *Small* **2010**, *6*, 2026−2034.

(29) Yu, Y.; Hessel, C.; Bogart, T.; Panthani, M.; Rasch, M.; Korgel, B. Room Temperature Hydrosilylation of Silicon Nanocrystals with Bifunctional Terminal Alkenes. *Langmuir* **2013**, *29*, 1533−1540.

(30) Tolstik, E.; Osminkina, L.; Akimov, D.; Gongalsky, M.; Kudryavstev, A.; Timoshenko, V.; Heintzmann, R.; Sivakov, V.; Popp, J. Linear and Non-Linear Optical Imaging of Cancer Cells with Silicon Nanoparticles. *Int. J. Mol. Sci.* **2016**, *17*, 1536−1550.

(31) Ravotto, L.; Chen, Q.; Vinogradov, S.; Locritani, M.; Bergamini, G.; Negri, F.; Yu, Y.; Korgel, B.; Ceroni, P. Bright Long-Lived Luminescence of Silicon Nanocrystals Sensitized by Two-Photon Absorbing Antenna. *Chem.* **2017**, *2*, 550−560.

(32) Tu, C.; Ma, X.; Pantazis, P.; Kauzlarich, S.; Louie, A. Paramagnetic, Silicon Quantum Dots for Magnetic Resonance and Two-Photon Imaging of Macrophages. *J. Am. Chem. Soc.* **2010**, *132*, 2016−2023.

(33) Park, J.-H.; Gu, L.; von Maltzahn, G.; Ruoslahti, E.; Bhatia, S. N.; Sailor, M. J. Biodegradable Luminescent Porous Silicon Nanoparticles for *In Vivo* Applications. *Nat. Mater.* **2009**, *8*, 331−336.

(34) Cao, Z.; Peng, F.; Hu, Z.; Chu, B.; Zhong, Y.; Su, Y.; He, S.; He, Y. *In Vitro* Cellular Behaviors and Toxicity Assays of Small-Sized Fluorescent Silicon Nanoparticles. *Nanoscale* **2017**, *9*, 7602−7611.

(35) Brus, L. Luminescence of Silicon Materials: Chains, Sheets, Nanocrystals, Nanowires, Microcrystals, and Porous Silicon. *J. Phys. Chem.* **1994**, *98*, 3575−3581.

(36) Mastronardi, M.; Henderson, E.; Puzzo, D.; Ozin, G. Small Silicon, Big Opportunities: The Development and Future of Colloidally-Stable Monodisperse Silicon Nanocrystals. *Adv. Mater.* **2012**, *24*, 5890−5898.

(37) Ramos, L.; Degoli, E.; Cantele, G.; Ossicini, S.; Ninno, D.; Furthmüller, J.; Bechstedt, F. Structural Features and Electronic Properties of Group-III-, Group-IV-, and Group-V-Doped Si Nanocrystallites. *J. Phys. Consens. Matter* **2007**, *19*, 466211.

(38) Ramos, L.; Weissker, H.; Furthmüller, J.; Bechstedt, F. Optical Properties of Si and Ge Nanocrystals: Parameter-Free Calculations. *Phys. Status Solidi B* **2005**, *242*, 3053−3063.

(39) Wen, X.; Zhang, P.; Smith, T.; Anthony, R.; Kortshagen, U.; Yu, P.; Feng, Y.; Shrestha, S.; Coniber, G.; Huang, S. Tunability Limit of Photoluminescence in Colloidal Silicon Nanocrystals. *Sci. Rep.* **2015**, *5*, 12469.

(40) Diener, J.; Kovalev, D.; Polisski, G.; Koch, F. Luminescence Properties of Two-Photon Excited Silicon Nanocrystals. *Opt. Mater.* **2001**, *17*, 117−120.

(41) Rumi, M.; Perry, J. Two-Photon Absorption: An Overview of Measurements and Principles. *Adv. Opt. Photonics* **2010**, *2*, 451−518.

(42) Basile, G.; Bergamin, A.; Cavagnero, G.; Mana, G.; Vittone, E.; Zosi, G. Measurement of the Silicon (220) Lattice Spacing. *Phys. Rev. Lett.* **1994**, *72*, 3133−3137.

(43) Du, H.; Fuh, R.; Li, J.; Corkan, L.; Lindsey, J. PhotochemCAD: A Computer-Aided Design and Research Tool in Photochemistry. *Photochem. Photobiol.* **1998**, *68*, 141−142.

(44) Makarov, N.; Drobizhev, M.; Rebane, A. Two-Photon Absorption Standards in the 550−1600 nm Excitation Wavelength Range. *Opt. Express* **2008**, *16*, 4029−4027.

(45) Furey, B.; Barba-Barba, R.; Carriles, R.; Bernal, A.; Mendoza, B.; Downer, M. Im$\{\chi^{(3)}\}$ Spectra of 110-Cut GaAs, GaP, and Si Near the Two-Photon Absorption Band Edge. *J. Appl. Phys.* **2021**, *129*, 183109.

(46) Bristow, A.; Rotenberg, N.; van Driel, H. Two-Photon Absorption and Kerr Coefficients of Silicon for 850−2200 nm. *Appl. Phys. Lett.* **2007**, *90*, 191104.

(47) Reintjes, J.; McGroddy, J. Indirect Two-Photon Transitions in Si at 1.06 μm. *Phys. Rev. Lett.* **1973**, *30*, 901−903.

(48) Dinu, M.; Quochi, F.; Garcia, H. Third-Order Nonlinearities in Silicon at Telecom Wavelengths. *Appl. Phys. Lett.* **2003**, *82*, 2954−2956.

(49) Euser, T.; Vos, W. Spatial Homogeneity of Optically Switched Semiconductor Photonic Crystals and of Bulk Semiconductors. *J. Appl. Phys.* **2005**, *97*, 043102.

(50) Tsang, H.; Wong, C.; Liang, T.; Day, I.; Roberts, S.; Harpin, A.; Drake, J.; Asghari, M. Optical Dispersion, Two-Photon Absorption and Self-Phase Modulation in Silicon Waveguides at 1.5 μm Wavelength. *Appl. Phys. Lett.* **2002**, *80*, 416−418.

(51) Reitze, D.; Zhang, T.; Wood, W.; Downer, M. Two-Photon Spectroscopy of Silicon Using Femtosecond Pulses at Above-Gap Frequencies. *J. Opt. Soc. Am. B* **1990**, *7*, 84−89.

(52) Murayama, M.; Nakayama, T. *Ab Initio* Calculations of Two-Photon Absorption Spectra in Semiconductors. *Phys. Rev. B* **1995**, *52*, 4986−4997.

(53) Ledoux, G.; Guillois, O.; Porterat, D.; Reynaud, C.; Huisken, F.; Kohn, B.; Paillard, V. Photoluminescence Properties of Silicon Nanocrystals As a Function of Their Size. *Phys. Rev. B* **2000**, *62*, 15942−15951.

(54) van Buuren, T.; Dinh, L.; Chase, L.; Siekhaus, W.; Terminello, L. Changes in the Electronic Properties of Si Nanocrystals as a Function of Particle Size. *Phys. Rev. Lett.* **1998**, *80*, 3803−3806.

(55) Furukawa, S.; Miyasato, T. Quantum Size Effects on the Optical Band Gap of Microcrystalline Si:H. *Phys. Rev. B* **1988**, *38*, 5726−5729.

(56) Hessel, C.; Reid, D.; Panthani, M.; Rasch, M.; Goodfellow, B.; Wei, J.; Fujii, H.; Akhavan, V.; Korgel, B. Synthesis of Ligand-Stabilized Silicon Nanocrystals with Size-Dependent Photoluminescence Spanning Visible to Near-Infrared Wavelengths. *Chem. Mater.* **2012**, *24*, 393−401.

(57) Ögüt, S.; Chelikowsky, J.; Louie, S. Quantum Confinement and Optical Gaps in Si Nanocrystals. *Phys. Rev. Lett.* **1997**, *79*, 1770−1773.

(58) Reboredo, F.; Franceschetti, A.; Zunger, A. Dark Excitons Due to Direct Coulomb Interactions in Silicon Quantum Dots. *Phys. Rev. B* **2000**, *61*, 13073−13087.

(59) Schnermann, M. Organic Dyes for Deep Bioimaging. *Nature* **2017**, *551*, 176−177.

(60) Strack, R. Organic Dyes for Live Imaging. *Nat. Methods* **2021**, *18*, 27−30.

(61) Hemmer, E.; Benayas, A.; Légaré, F.; Vetrone, F. Exploiting the Biological Windows: Current Perspectives on Fluorescent Bioprobes Emitting Above 1000 nm. *Nanoscale Horiz* **2016**, *1*, 168−184.

(62) Pu, S.; Yang, M.; Hsu, C.; Lai, C.; Hsieh, C.; Lin, S.; Cheng, Y.; Chou, P. The Empirical Correlation Between Size and Two-Photon Absorption Cross Section of CdSe and CdTe Quantum Dots. *Small* **2006**, *2*, 1308−1313.

(63) Padilha, L.; Fu, J.; Hagan, D.; Van Stryland, E.; Cesar, C.; Barbosa, L.; Cruz, C.; Buso, D.; Martucci, A. Frequency Degenerate and Nondegenerate Two-Photon Absorption Spectra of Semiconductor Quantum Dots. *Phys. Rev. B* **2007**, *75*, 075325.

(64) Cai, Y.; Wei, Z.; Song, C.; Tang, C.; Han, W.; Dong, X. Optical Nano-Agents in the Second Near-Infrared Window for Biomedical Applications. *Chem. Soc. Rev.* **2019**, *48*, 22−37.

(65) Borsella, E.; D'Amato, R.; Falconieri, M.; Trave, E.; Panariti, A.; Rivolta, I. An Outlook on the Potential of Si Nanocrystals As Luminescent Probes for Bioimaging. *J. Mater. Res.* **2013**, *28*, 193−204.

(66) Smith, A.; Mancini, M.; Nie, S. Second Window for *In Vivo* Imaging. *Nat. Nanotechnol* **2009**, *4*, 710−711.

(67) Friebel, M.; Helfmann, J.; Netz, U.; Meinke, M. Influence of Oxygen Saturation on the Optical Scattering Properties of Human Red Blood Cells in the Spectral Range 250 to 2000 nm. *J. Biomed. Opt.* **2009**, *14*, 034001.

(68) Bashkatov, A.; Genina, E.; Kochubey, V.; Tuchin, V. Optical Properties of Human Skin, Subcutaneous and Mucous Tissues in the Wavelength Range from 400 to 2000 nm. *J. Phys. D: Appl. Phys.* **2005**, *38*, 2543.

(69) Xu, C.; Webb, W. Measurement of Two-Photon Excitation Cross Sections of Molecular Fluorophores with Data from 690 to 1050 nm. *J. Opt. Soc. Am. B* **1996**, *13*, 481−491.

(70) Shapiro, H. Excitation and Emission Spectra of Common Dyes. *Current Protocols in Cytometry* **2003**, *26*, 1.19.1−1.19.7.

(71) Schmitt, A.; Hikeldey, B.; Wild, M.; Jung, G. Synthesis of the Core Compound of the BODIPY Dye Class: 4,4'-difluoro-4-bora-(3a,4a)-diaza-s-indacene. *J. Fluoresc.* **2009**, *19*, 755−758.

(72) Mannekutla, J.; Mulimani, B.; Inamdar, S. Solvent Effect on Absorption and Fluorescence Spectra of Coumarin Laser Dyes: Evaluation of Ground and Excited State Dipole Moments. *Spectrochimica Acta Part A: Molecular and Biomolecular Spectroscopy* **2008**, *69*, 419−426.

(73) Johnson, I., Spence, M., Eds. *Molecular Probes Handbook: A Guide to Fluorescent Probes and Labeling Technologies*, 11th ed.; Life Technologies: New York, 2010; pp 57−65.

(74) *Lucifer Yellow CH*. https://omlc.org/spectra/PhotochemCAD/html/065.html, Accessed: 2021-07.

(75) Casey, K.; Quitevis, E. Effect of Solvent Polarity on Nonradiative Processes in Xanthene Dyes: Rhodamine B in Normal Alcohols. *J. Phys. Chem.* **1988**, *92*, 6590−6594.

(76) Kedenburg, S.; Vieweg, M.; Gissibl, T.; Giessen, H. Linear Refractive Index and Absorption Measurements of Nonlinear Optical

Liquids in the Visible and Near-Infrared Spectral Region. *Opt. Mater. Express* **2012**, *2*, 1588−1611.

https://doi.org/10.1021/acsnano.1c11428